Visual Servo Aircraft Control for Tracking Parallel Curves

Pedro Serra, Rita Cunha

Abstract— **This paper describes a nonlinear Image-Based Visual Servo (IBVS) controller for tracking nonlinear parallel 2-D curves, such as catenaries, with a fixed-wing aircraft. Image features are exploited from the image of the lines to design a feedback controller for the automatic manoeuvre. For curves in the vertical plane the proposed solution guarantees exponential stability in the horizontal direction and ultimate boundedness in the vertical direction, with bound proportional to the slope deviation with respect to a straight line. Simulation results are presented to illustrate the performance of the control approach.**

I. Introduction

Over the last decade, a growing interest in unmanned aerial vehicles (UAVs) has spread among the research community. Their potential to perform high precision tasks in challenging and uncertain operation scenarios is a motivation for the increasing effort on the development of new control algorithms. Moreover, the new sensor technology and the increasingly powerful computational systems are potentiating new and more challenging applications.

Inspection of infrastructures, such as bridges [1] or chimneys [2], has spawned a wide range of application with major interest within the research community where the use of cameras arises as natural tool for automatic inspection.

The research and development in the area of unmanned aerial vehicles has been paying off due to the many advantages when comparing to the traditional technologies that require man presence and intervention, such as

- reduce costs by decreasing the need of manpower;
- reduce costs by decreasing the energy dependence;
- improve reliability of the results in some cases where human errors are frequent;
- give access to areas that are out-of-range for manned vehicles;
- expand the range of applications, including in indoor environments due to high manoeuvrability and small size;
- reduce risks of accidents and injuries.

The measurement of the vehicle's position with respect to the local environment is a major problem when designing control systems. Global Positioning System (GPS) is being widely used as the primary navigation aid, however there has been an increasing interest in developing alternative systems that provide robust relative pose information to be used in navigation algorithms. One alternative is the use of a vision system. Using cameras as primary sensors for relative position, the flight control problem can be cast into an Image-Based Visual Servo (IBVS) Control problem ([3], [4]), opening the possibility to perform autonomous tasks in low-structured environments with no external assistance, [5], [6].

This paper presents a solution to the problem of tracking nonlinear parallel 2-D curves, in particular, the typical catenary curve described by the overhead power lines. The proposed controller borrows from the work in [6], where the authors present an IBVS controller to track parallel straight lines, using the normalized Plücker coordinates of the straight lines, which can be readily obtained from the image measurements. The landing manoeuvre of an airplane is approached in [7] and [8], where the presented solution is also based in the Plücker coordinates of the lines delimiting the runway complemented with the Optical-Flow for the Flare phase. In this paper, we consider a modified version of the image error introduced in [6] that can be used for non-straight lines and is obtained by combining information from the vanishing point where the curves meet, with the image coordinates of points on the curves, which are judiciously chosen. For curves in the vertical plane, the proposed solution guarantees uniform exponential stability in the horizontal direction and ultimate boundedness in the vertical direction. The bound on this error is proportional to the maximum relative slope of the tangent to the curves, with the zero-slope direction defined by the vanishing point.

The control architecture is decoupled into an inner-loop and outer-loop controller. The outer-loop controller stabilizes the translational (or guidance) dynamics resorting to visual data and using the roll angle and the angle of attack as control inputs. The inner-loop controller actuates on the aircraft control surfaces and provides high-gain stabilization of the vehicle's angle of attack, side-slip and roll angles based on direct measurements of the IMU and pitot tubes. The time-scale separation between the two loops is considered sufficient so that the interaction terms can be ignored in the control design. Detailed studies on the inner/outer loop approach of controllers design can be found in [9] and [10].

This paper is structured in four sections. Section II presents the dynamic model of an airplane. Section III presents the image features that are used in the control design which, in turn, is presented in section IV. Section V presents simulation results for the full nonlinear dynamics of an aircraft. The final section provide a short summary of conclusions and future research directions.

II. Modelling

A. Aircraft dynamics

This section briefly describes the aircraft dynamic model adopted. For a comprehensive coverage of aircraft flight dynamics, the reader is referred to [11].

Let $\{\mathcal{I}\}$ denote the inertial reference frame and $\{\mathcal{B}\}$ the body reference frame, attached to the vehicle's center of mass. Furthermore, two additional reference frames attached to the vehicle's center of mass are introduced, the airspeed reference frame $\{\mathcal{W}\}$ and the stability reference frame $\{\mathcal{S}\}$, see Fig. 1. The angle of attack α, defines the orientation of the stability coordinate frame $\{\mathcal{S}\}$, which is used for analysing the effect of perturbations from steady-state flight.

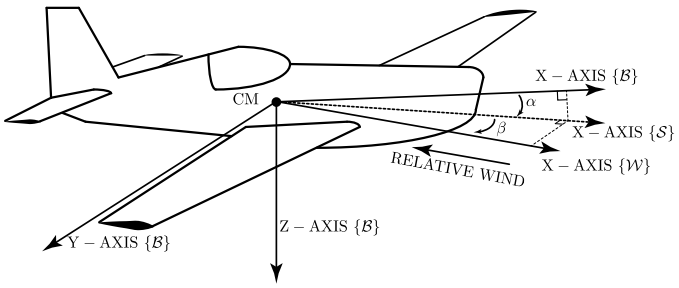

Fig. 1. Reference frames.

The airspeed coordinate frame $\{\mathcal{W}\}$ is obtained from the stability coordinate frame through a rotation about the z-axis by the side-slip angle β. Therefore, the rotation matrices from $\{\mathcal{S}\}$ to $\{\mathcal{W}\}$ and from $\{\mathcal{B}\}$ to $\{\mathcal{S}\}$ are given, respectively, by

$$ {}^{\mathcal{W}}_{\mathcal{S}}R = R_Z(-\beta), \qquad {}^{\mathcal{S}}_{\mathcal{B}}R = R_Y(\alpha). \tag{1} $$

The flight-path, heading, and bank angles (γ, χ, μ) are the so called wind angles and describe the orientation of the airspeed frame with respect to the inertial frame, such that

$$ {}^{\mathcal{I}}_{\mathcal{W}}R = R_Z(\chi)R_Y(\gamma)R_X(\mu). \tag{2} $$

Assuming the presence of wind with velocity v_w expressed in $\{\mathcal{I}\}$, let v_b denote the velocity of the aircraft relative to the wind expressed in $\{\mathcal{B}\}$, and let v denote the same vector expressed $\{\mathcal{I}\}$. Let $\Omega = (p, q, r)^T$ denote the angular velocity also expressed in $\{\mathcal{B}\}$, $\xi = (x, y, z)^T$ the position in $\{\mathcal{I}\}$ and $R = {}^{\mathcal{I}}_{\mathcal{B}}R$ the rotation matrix from $\{\mathcal{B}\}$ to $\{\mathcal{I}\}$. For fixed-wing aircraft, it is convenient to write the equations of motion using a state vector naturally suited for flight control design. Instead of v_b, the variables V, α, and β are used to describe the magnitude and direction of the relative airspeed, which according to (1) satisfy

$$ v_b = {}^{\mathcal{B}}_{\mathcal{W}}R \begin{bmatrix} V \\ 0 \\ 0 \end{bmatrix} = V \begin{bmatrix} \cos\beta\cos\alpha \\ \sin\beta \\ \cos\beta\sin\alpha \end{bmatrix}. \tag{3} $$

In addition, the wind angles (γ, χ, μ), used to describe the orientation of the vehicle are related with the relative velocity expressed in $\{\mathcal{I}\}$. According to (2)

$$ v = {}^{\mathcal{I}}_{\mathcal{W}}R \begin{bmatrix} V \\ 0 \\ 0 \end{bmatrix} = V \begin{bmatrix} \cos\chi\cos\gamma \\ \sin\chi\cos\gamma \\ -\sin\gamma \end{bmatrix}. \tag{4} $$

Therefore, the dynamic and kinematic equations of motion for the aircraft can be written as

$$ I\dot{\Omega} = -\mathrm{s_k}(\Omega)\, I\Omega + \Gamma \tag{5} $$

$$ \dot{\xi} = v + v_w \tag{6} $$

$$ \dot{R} = R\mathrm{s_k}(\Omega) \tag{7} $$

$$ \dot{V} = \frac{1}{m}\left(F_T\cos\alpha\cos\beta - D\right) - g\sin\gamma \tag{8} $$

$$ \dot{\beta} = -\frac{1}{mV}(F_T\cos\alpha\sin\beta + C) + \frac{1}{m}g\sin\mu\cos\gamma - r_s \tag{9} $$

$$ \begin{aligned} \dot{\alpha} = &-\frac{1}{mV\cos\beta}(F_T\sin\alpha + L) + \frac{1}{V\cos\beta}g\cos\mu\cos\gamma + \\ &+ (q - p_s\tan\beta) \end{aligned} \tag{10} $$

$$ \begin{aligned} \dot{\gamma} &= -\tfrac{1}{V}g\cos\gamma + \tfrac{1}{mV}(C\sin\mu + L\cos\mu) + \\ &+ \tfrac{F_T}{mV}\left[\sin\alpha\cos\mu + \cos\alpha\sin\beta\sin\mu\right] \end{aligned} \tag{11} $$

$$ \begin{aligned} \dot{\chi} &= \tfrac{1}{mV\cos\gamma}(L\sin\mu - C\cos\mu) + \\ &+ \tfrac{F_T}{mV\cos\gamma}\left[\sin\alpha\sin\mu - \cos\alpha\sin\beta\cos\mu\right] \end{aligned} \tag{12} $$

$$ \begin{aligned} \dot{\mu} &= L\left[\tan\beta + \tan\gamma\sin\mu\right]/(mV) + \\ &- C\tan\gamma\cos\mu/(mV) + \\ &+ F_T\left[\sin\alpha\sin\mu\tan\gamma + \sin\alpha\tan\beta\right]/(mV) + \\ &- F_T\cos\alpha\sin\beta\cos\mu\tan\gamma/(mV) + \\ &- \cos\alpha\sin\beta\cos\mu\tan\gamma/(mV) + \\ &+ \tfrac{p_s}{mV\cos\beta} - \tfrac{g}{V}\tan\beta\cos\gamma\cos\mu \end{aligned} \tag{13} $$

where m is vehicle's mass, I the moment of inertia, Γ the exogenous torque, F_T is the thrust input and g the gravitational acceleration. The aerodynamic force components due to the drag, D, crosswind C and lift L are described by

$$ \begin{bmatrix} -D \\ -C \\ -L \end{bmatrix} = \bar{q}SR_Z(-\beta) \begin{bmatrix} C_D \\ C_Y \\ C_L \end{bmatrix} \tag{14} $$

where $\bar{q} = \frac{1}{2}\rho V^2$ is the dynamic pressure, ρ is the density of the air. Assuming that the vehicle is operating close to a trimming condition, the stability-coefficients can be described by

$$ \begin{aligned} C_D &= C_{D_0} + C_{D_\alpha}\Delta_\alpha \\ C_Y &= C_{Y_\beta}\beta + \tfrac{b}{2V}\left(C_{Y_p}p + C_{Y_r}r\right) + C_{Y_{\delta_r}}\delta_r \\ C_L &= C_{L_0} + C_{L_\alpha}\Delta_\alpha + \tfrac{\bar{c}}{2V}C_{L_q}q + C_{L_{\delta_e}}\delta_e. \end{aligned} \tag{15} $$

where δ_e, δ_a, and δ_r denote the elevator, aileron, and rudder angles, respectively. To complete the model, the exogenous moments in (5) can be written as $\Gamma = \bar{q}S(bC_l, \bar{c}C_m, bC_n)^T$ and

$$ \begin{aligned} C_l &= C_{l_0} + C_{l_\beta}\beta + \tfrac{b}{2V}\left(C_{l_p}p + C_{l_r}r\right) + C_{l_{\delta_r}}\delta_r + C_{l_{\delta_a}}\delta_a \\ C_m &= C_{m_0} + C_{m_\alpha}\Delta_\alpha + \tfrac{\bar{c}}{2V}C_{m_q}q + C_{m_{\delta_e}}\delta_e \\ C_n &= C_{n_\beta}\beta + \tfrac{b}{2V}\left(C_{n_p}p + C_{n_r}r\right) + C_{n_{\delta_r}}\delta_r + C_{n_{\delta_a}}\delta_a \end{aligned} \tag{16} $$

Note that the airplane should not be used when the wind conditions are higher than a limit identified upon the airplane conception. Hence, the following assumption is done on wind velocity.

Assumption 1: There exists $\varepsilon \in [0, 1]$ such that:

$$ \|v_w\| < \varepsilon V. \tag{17} $$

The airplane considered in this paper, is a $1/4$ scale Extra-330 since it is a highly aerobatic aircraft. The parameters for this aircraft were found resorting to a wind tunnel simulator and are presented in Table I.

B. The Inner-Loop

The inner-loop is designed resorting to time-scale separation, that allows the partitioning of the aircraft dynamics into slow states and fast states, with the fast states used as controls for the slow states, [12]. Fig. 2 shows the block diagram of the inner loop. The references to the inner-loop are the desired angle of attack, sideslip and bank angles (see Fig. 2).

The propulsion controlled uses the thrust command in equation (8) to drive the norm of the airspeed to a desired constant value.

The surface controller is designed in order to drive the angular velocity Ω to a desired velocity Ω^d, using the control surfaces δ_e, δ_a and δ_r in equation (5).

TABLE I
MODEL-SPECIFIC PARAMETERS AND COEFFICIENTS.

Longitudinal		Lateral-directional	
C_{D_0}	0.03245	C_{Y_β}	-0.2727
C_{D_α}	0.0863	C_{Y_p}	0.0194
C_{L_0}	0.1426	C_{Y_r}	0.2531
C_{L_α}	3.7007	C_{l_β}	-0.0314
C_{L_q}	3.5927	C_{l_p}	-0.5858
C_{m_α}	-0.2850	C_{l_r}	0.07427
C_{m_q}	-4.3732	C_{n_β}	0.1052
		C_{n_p}	-0.03874
		C_{n_r}	-0.1156
Elevator		Rudder	
$C_{L_{\delta_e}}$	0.3976	$C_{Y_{\delta_r}}$	0.2228
$C_{m_{\delta_e}}$	-0.7572	$C_{l_{\delta_r}}$	0.02194
		$C_{n_{\delta_r}}$	-0.1003
		Aileron	
		$C_{l_{\delta_a}}$	0.3707
		$C_{n_{\delta_a}}$	-0.008
Geometric Data			
I_{xx}, kg.m^2	1.4759	S, m^2	1.0126
I_{yy}, kg.m^2	2.8563	b, m	2.4079
I_{zz}, kg.m^2	4.1190	$\bar{c}$, m	0.4420
I_{xz}, kg.m^2	0	m, kg	12.7459
α_0, deg	1	$V, m/s$	36.0111

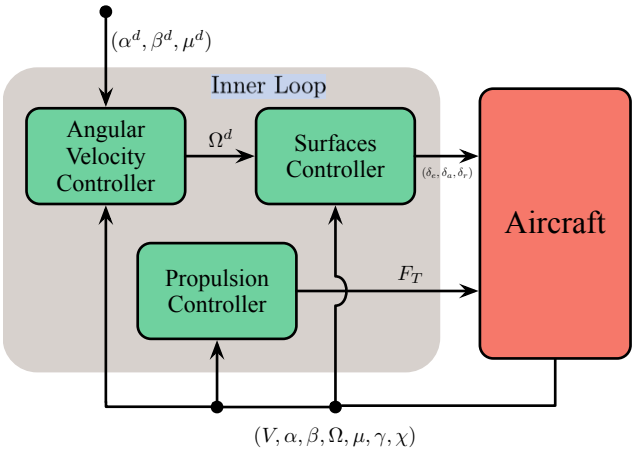

Fig. 2. Inner-Loop diagram.

The angular velocity controller, uses Ω^d as control input in equations (9), (10) and (13) in order to drive the angles α, β and μ to the desired values given as references by the outer-loop.

Since the inner-loop design is not the main issue addressed by this paper, the inerested reader is refered to [12] and [13].

C. The outer-loop

The outer-loop has to deal with the guidance dynamics which were left uncontrolled by the inner-loop, namely the dynamics of the flight-path angle γ and of the heading angle χ, which according to (4) define the direction of the relative velocity vector expressed in $\{\mathcal{I}\}$.

Hence, considering that V is constant it is possible to write the velocity dynamics as

$$\dot{v} = \mathrm{s_k}\,(v)\, R_z(\chi) \begin{bmatrix} 0 & 0 \\ 1 & 0 \\ 0 & 1 \end{bmatrix} \begin{bmatrix} \dot{\gamma} \\ \dot{\chi} \end{bmatrix} \tag{18}$$

where $\dot{\gamma}$ and $\dot{\chi}$ are presented in equations (11) and (12) respectively.

For the application in hand, it is more suited to use the bank-to-turn manoeuvre and therefore the sideslip angle β must be driven to zero. The reference for the desired sideslip angle passed to the inner loop is, then, $\beta^d = 0$. Finally, the guidance dynamics can be described by

$$\dot{v} = \frac{1}{mV} \mathrm{s_k}\,(v)\, u_a(0, \alpha^d, \mu^d) \tag{19}$$

where the function $u_a(.)$ is obtained from (18) assuming that V is constant and $\beta = 0$. $u_a(.)$ is used as a virtual control input to be used by the IBVS algorithm presented in the next sections. α^d and μ^d are obtained from the non-linear inversion of $u_a(.)$.

III. VISUAL FEATURES

The goal of this paper is to introduce a new technique for tracking non-straight lines in 3D space based on visual features. For a better understanding of this methodology, it is convenient to first consider the simpler case of tracking straight lines.

A. Vision-based tracking of straight lines

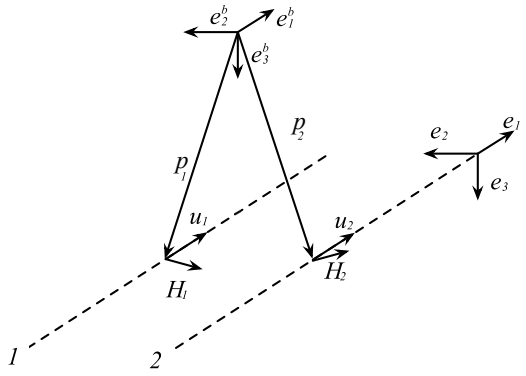

Fig. 3. Parallel lines and Plücker coordinates.

Consider a set of $n \geq 2$ straight lines, as illustrated in Fig. 3, with unit direction described by u expressed in $\{\mathcal{I}\}$[1]. Consider also a point on the line i ($i = 1, 2, \ldots, n$), l_i expressed in $\{\mathcal{I}\}$. Each line can be described in a convenient way resorting to the Plücker coordinates, [6], [7], [8], which comprise the direction u and the vector H_i given by

$$H_i = p_i \times u, \tag{20}$$

where $p_i = l_i - \xi$. Although H_i cannot be extracted directly from the image, it is possible to obtain a normalization of this variable, [6], (as detailed further ahead)

$$h_i = H_i / \|H_i\|. \tag{21}$$

Suppose the goal is to steer the airplane along the direction u, keeping a constant position with respect to the lines. One possible solution to this problem relies on a single image feature given by the centroid

$$q = \sum h_i. \tag{22}$$

[1]Assume, for now, that this vector is known. In fact, it can be extracted from the image using different methods that are presented further ahead.

As required, q encodes all the information about the position of the vehicle with respect to the straight lines, apart from the coordinate along the direction u (see [6] for further details). Hence, to achieve the tracking objective, we can define the error to be driven to zero through a feedback control system as

$$\delta := q - q^* \tag{23}$$

where q^* is constant in $\{\mathcal{I}\}$ defined as desired centroid. Figure 4 shows some possible positions for the airplane and the corresponding measured centroids.

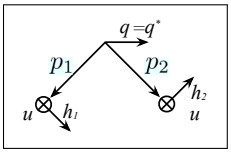

(a) Airplane in the center of the two lines.

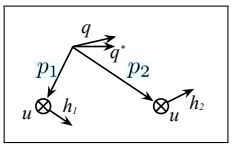

(b) Airplane slightly to the left.

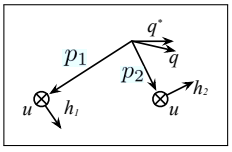

(c) Airplane slightly to the right.

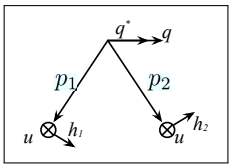

(d) Airplane slightly above the desired position.

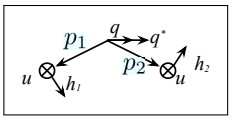

(e) Airplane slightly below the desired position.

Fig. 4. Different positions and respective centroid measurements.

B. Vision-based tracking of nonlinear curves

Consider a set of $n \geq 2$ nonlinear parallel curves, whose coordinates in $\{\mathcal{I}\}$ can be parametrized by a scalar τ such that

$$\bar{l}_i(\tau) = u\tau + \sigma(\tau)u_0 + l_{i0} \tag{24}$$

where $\sigma(\tau)$ is a bounded scalar function with bounded derivative, u_0 and l_{i0} are constant vectors in $\mathbb{R}^3$, and u_0 satisfies $u^T u_0 = 0$. In particular, we are interested in catenary lines of the form

$$\bar{l}_i(\tau) = (\tau, l_{iy}, -a\cosh\{[\tau - (\text{ceil}(\tau/L) - 1)L - L/2]/a\})^T, \tag{25}$$

where l_{iy} and a are constant scalars, L is the length of the line and $\text{ceil}(.)$ is the round toward positive infinity. For this particular case, we have $u = [1\ 0\ 0]^T$, $u_0 = [0\ 0\ 1]^T$, $l_{i0} = [0\ l_{iy}\ 0]^T$, and $\sigma(\tau) = -a\cosh\{[\tau - (\text{ceil}(\tau/L) - 1)L - L/2]/a\}$. Typically, this is the equation obeyed by electric power lines between towers, see Figure 5.

Consider the plane that passes through the aircraft's current position ξ and is perpendicular to u. The point of intersection between this plane and each line i ($i = 1, 2, \ldots, n$) can be obtained with $\tau_\xi = -u^T(l_{i0} - \xi)$ and has coordinates in $\{\mathcal{B}\}$ given by

$$\begin{aligned} \bar{p}_i &= \bar{l}_i(\tau_\xi) - \xi \\ &= \pi_u(l_{i0} - \xi) + \sigma(\tau_\xi)u_0 \end{aligned} \tag{26}$$

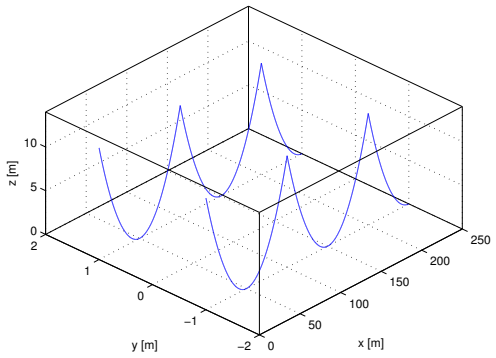

Fig. 5. Catenary lines.

where π_x denotes the projection matrix given by

$$\pi_x = I - \frac{xx^T}{\|x\|^2}. \tag{27}$$

Following the line of thought used for straight lines, consider the vectors $\bar{H}_i = \bar{p}_i \times u$ and $\bar{h}_i = \bar{H}_i/\|\bar{H}_i\|$, which can be associated to the Plucker coordinates of virtual straight lines passing through each $\bar{p}_i$ and with direction u. Consider also a new single image feature given by $\bar{q} = \sum \bar{h}_i$ and finally the new error $\bar{\delta} = \bar{q} - q^*$.

C. Extracting the visual features from the image information

Considering the case where parallel straight lines are being viewed by the camera, the normalized Plücker coordinates h_i can be extracted using the external product between two points in the same line

$$h_i = R\frac{im(P_i^1) \times im(P_i^2)}{\|im(P_i^1) \times im(P_i^2)\|}, \tag{28}$$

where $im(P_i^j) = P_i^j/\|P_i^j\|$ denotes the image of P_i^j for an ideal spherical camera and P_i^j denotes the 3-D coordinates of a point j on the line i, expressed in the body frame $\{\mathcal{B}\}$. Notice that $im(P_i^j)$ can be readily obtained from the image acquired using a calibrated CCD camera.

Since u is orthogonal to each h_i, it can be written as

$$u = \frac{h_1 \times h_2}{\|h_1 \times h_2\|}. \tag{29}$$

Consider now the case where the lines are not straight. Although (29) no longer holds, we can still extract the direction u from the image, using the vanishing point where the lines meet [14]. Assuming that the vanishing point is visible in image plane, it can be shown that it represents a direct measure of u, since

$$u = R\lim_{\tau\to\infty} im(R^T(\bar{l}_i(\tau) - \xi)), \tag{30}$$

where $\bar{l}_i(\tau)$ describes the line coordinates in $\{\mathcal{I}\}$, as introduced in (24). Then, the vectors $\bar{h}_i$ can be obtained using

$$\bar{h}_i = R\frac{im(\bar{P}_i) \times R^T u}{\|im(\bar{P}_i) \times R^T u\|}, \tag{31}$$

with $\bar{P}_i = R^T\bar{p}_i$.

IV. CONTROL

Considering, for now, that the wind velocity is negligible, the dynamics of the points p_i can be described by

$$\dot{p}_i = -v_t, \tag{32}$$

where $v_t = v + v_w$, and the dynamics of the normalized Plücker coordinates are given by

$$\dot{h}_i = \frac{1}{\|H_i\|}\pi_{h_i}\mathrm{s_k}(u)\, v_t. \tag{33}$$

Then, for the case of straight lines, the dynamics of the error δ can be described by

$$\dot{\delta} = Q\mathrm{s_k}(u)\, v_t \tag{34}$$

where the image Jacobian matrix Q is given by

$$Q = \sum \frac{1}{\|H_i\|}\pi_{h_i}. \tag{35}$$

It is not possible to extract $\|H_i\|$ directly from the image, therefore the measurement of the matrix Q is a difficult task. Nonetheless, as carefully described in [6], it is always possible to define Q as a positive definite matrix, which allows for the synthesis of controllers without an explicit estimate of Q. However, the trajectories considered must be subject to some bounds in order to avoid ill-conditioning of the control system. Hence, a region of space is defined by a pair of uniform bounds on the matrix Q, [6]

$$\lambda_{\min}(Q) < \{\lambda_i(Q)\} < \lambda_{\max}(Q). \tag{36}$$

For the case of nonlinear curves, the time derivative of $\bar{p}_i$ can be written as

$$\dot{\bar{p}}_i = -\pi_u v_t + \frac{\partial\sigma(\tau_\xi)}{\partial\tau}u_0 u^T v_t, \tag{37}$$

where $\tau_\xi = -u^T(l_{i0} - \xi)$. The partial derivative $\frac{\partial\sigma(\tau_\xi)}{\partial\tau}$ is unknown since the position of the aircraft relatively to the lines is unknown.

Using (37) to compute $\dot{H}_i$ and consequently $\dot{\bar{h}}_i$, it follows that

$$\dot{\bar{\delta}} = Q\mathrm{s_k}(u)\,(I - \frac{\partial\sigma(\tau_\xi)}{\partial\tau}u_0 u^T)v_t. \tag{38}$$

A comparison between (38) and (34) highlights the fact that $\bar{\delta}$ can be interpreted as a generalization of δ, since (38) reduces to (34) when the lines are straight, or, equivalently, when $\frac{\partial\sigma(\tau_\xi)}{\partial\tau} = 0$. In view of this result, we proceed with the design of a control law for the general case of nonlinear curves, which is also applicable to straight lines.

Let $\hat{v}_w$ be an estimate of $v_w \times u$, therefore, $\tilde{v}_w = v_w \times u - \hat{v}_w$. Choose the following dynamics for $\hat{v}_w$

$$\dot{\hat{v}}_w = \mathbf{P}\pi_u u_w \tag{39}$$

where u_w acts as the innovation of the wind estimator and

$$\mathbf{P} = \varepsilon' V\sqrt{1 - \frac{\|\hat{v}_w\|^2}{\varepsilon'^2 V^2}}\left(I - \frac{\hat{v}_w \hat{v_w}^T}{\varepsilon'^2 V^2}\right), \quad \varepsilon' \in \left(\frac{1+\varepsilon}{2}, 1\right). \tag{40}$$

Choosing the innovation term of the wind estimate, u_w, as $u_w = -k_2\bar{\delta}$ with $k_2 > 0$ and given that the error dynamics (38) has no actuation input, let v_d be the desired velocity defined as

$$v_d = \mathrm{s_k}(u)\,(k_1\bar{\delta} - \hat{v}_w) + u\sqrt{V^2 - \|k_1\bar{\delta} - \hat{v}_w\|^2}, \tag{41}$$

and consider the new error term given by

$$\delta_v = \mathrm{s_k}(u)\,(v - v_d). \tag{42}$$

Using (42), the error dynamics can be rewritten as

$$\dot{\bar{\delta}} = -k_1 Q\bar{\delta} - Q\tilde{v}_w + Q\delta_v - Q\mathrm{s_k}(u)\frac{\partial\sigma(\tau_\xi)}{\partial\tau}u_0 u^T v_t \tag{43}$$

and with (19)

$$\begin{aligned}\dot{\delta}_v \;&= -\tfrac{1}{mV}\mathrm{s_k}(u)\,\mathrm{s_k}(v)\,u_a + k_1 Q\delta_v - k_1^2 Q\bar{\delta} + \\ &\quad -k_1\mathrm{s_k}(u)\,Q\mathrm{s_k}(u)\,\tfrac{\partial\sigma(\tau_\xi)}{\partial\tau}u_0 u^T v_t - k_2\mathrm{s_k}(u)\,\mathbf{P}\bar{\delta}\end{aligned} \tag{44}$$

The following theorem shows that if $\sigma(\tau)$ has a bounded derivative the state $(\bar{\delta}, \delta_v, \tilde{v}_w)$ is uniformly ultimately bounded.

Theorem 1: Consider the dynamics given by (43) and (44) and assume that $|\frac{\partial\sigma(\tau)}{\partial\tau}| \leq c_0$, for all $\tau \in \mathbb{R}$, the initial velocity satisfies $v(0)^T u > 0$, the desired position is the middle of the curves, i.e.

$$\frac{q^*}{\|q^*\|} = \mathrm{s_k}(u)\,u_0. \tag{45}$$

Then, with gains K, k_1, k_2 and k_3 that satisfy

$$K < \frac{2}{k_1} \tag{46}$$

$$\frac{\lambda_{\max}(Q)}{\lambda_{\min}(Q)} < k_1 < \frac{V}{2\max\{\|\bar{\delta}\|\}} \tag{47}$$

$$k_2 < k_1\frac{\lambda_{\min}(Q) - 2\lambda_{\max}(Q)}{2\varepsilon' V} \tag{48}$$

$$k_3 > \frac{k_2}{2}\varepsilon' V + \left(\frac{k_1^2}{2} + \frac{1}{K} + k_1\right)\lambda_{\max}(Q) \tag{49}$$

the control law

$$u_a = -k_3\frac{mV}{v^T u}\delta_v \tag{50}$$

ensures uniform ultimate boundedness of the solution $(\bar{\delta}(t), \delta_v(t))$, with bound given by

$$b = \frac{c_0\lambda_{\max}(Q)Vk_1}{\rho(k_1\lambda_{\min}(Q) - 1)},\ 0 < \rho < 1. \tag{51}$$

Proof: Consider the Storage function given by

$$S_1 = \|\bar{\delta}\|^2 + \frac{2}{k_1}\tilde{v}_w^T\bar{\delta} + \frac{4}{k_1^2}\|\tilde{v}_w\|^2. \tag{52}$$

Its derivative can by written as

$$\begin{aligned}\dot{S}_1 \;&= 2\left(\bar{\delta} + \tfrac{\tilde{v}_w}{k_1}\right)^T Q\delta_v + \tfrac{2k_2}{k_1}\left(\bar{\delta} + 4\tfrac{\tilde{v}_w}{k_1}\right)^T\mathbf{P}\delta + \\ &\quad -2k_1\left(\bar{\delta} + \tfrac{\tilde{v}_w}{k_1}\right)^T + \\ &\quad -2\left(\bar{\delta} + \tfrac{\tilde{v}_w}{k_1}\right)^T Q\mathrm{s_k}(u)\,\tfrac{\partial\sigma(\tau_\xi)}{\partial\tau}u_0 u^T v_t\end{aligned} \tag{53}$$

Applying the control law (50) to the first term of (44) yields

$$-\frac{1}{mV}\delta_v^T\mathrm{s_k}(v)\,u_a = -k_3\|\delta_v\|^2, \tag{54}$$

hence, let S_2 be a second Storage function given by

$$S_2 = \frac{K}{2}\|\delta_v\|^2. \tag{55}$$

The derivative is given by

$$\begin{aligned}\dot{S}_2 \;&= -k_3 K\|\delta_v\|^2 + Kk_1^2\delta_v^T\mathrm{s_k}(u)\,Q\left(\bar{\delta} + \tfrac{\tilde{v}_w}{k_1}\right) + \\ &\quad -Kk_1\delta_v^T\mathrm{s_k}(u)\,Q\delta_v - Kk_2\delta_v^T\mathrm{s_k}(u)\,\mathbf{P}\bar{\delta} + \\ &\quad +Kk_1\delta_v^T\mathrm{s_k}(u)\,Q\mathrm{s_k}(u)\,\tfrac{\partial\sigma(\tau_\xi)}{\partial\tau}u_0 u^T v_t\end{aligned} \tag{56}$$

Now consider a Lyapunov function given by $\mathcal{L} = S_1 + S_2$. Applying the Cauchy-Swartz inequality, the derivative of $\mathcal{L}$ can be upper bounded by

$$\begin{aligned}\dot{\mathcal{L}} \quad &\leq \left(\bar{\delta} + \tfrac{\tilde{v}_w}{k_1}\right)^T \left(-k_1 Q + 2\tfrac{k_2}{k_1}\mathbf{P} + Q\left(1 + \tfrac{Kk_1}{2}\right)\right)\left(\bar{\delta} + \tfrac{\tilde{v}_w}{k_1}\right) \\ &+\delta_v^T \left(-k_3 KI + \tfrac{Kk_2}{2}\mathbf{P} + \left(\tfrac{Kk_1^2}{2} + 1 - Kk_1\right)Q\right)\delta_v \\ &-k_2 \bar{\delta}^T \mathbf{P}\bar{\delta}\left(\tfrac{1}{k_1} - \tfrac{K}{2}\right) + \\ &+ \left(Kk_1\|\delta_v\| + 2\|\bar{\delta}\| + 2\tfrac{\|\tilde{v}_w\|}{k_1}\right)\lambda_{\max}(Q)c_0(1+\varepsilon)V \end{aligned} \tag{57}$$

Therefore the system is uniformly ultimately bounded provided that the gains K, k_1, k_2 and k_3 satisfy (46), (47) , (48) and (49).

It remains to be proven that $v(t)^T u > 0$ for all $t > t_0$. Consider the following storage function

$$S = V - v^T u = \frac{1}{2V}\|v - Vu\|^2. \tag{58}$$

The derivative is given by

$$\dot{S} = -\frac{k_3}{v^T u}(V + v^T u)S + \frac{k_1 k_3}{v^T u}(v - Vu)^T \mathrm{S_k}(u)\,\bar{\delta} \tag{59}$$

and can be upper bounded by

$$\dot{S} \leq -\frac{k_3}{v^T u}\|v - Vu\|\left(\frac{1}{2V}(V + v^T u)\|v - Vu\| - k_1\|\bar{\delta}\|\right) \tag{60}$$

which is negative definite as long as $k_1^2\|\bar{\delta}\|^2 \leq \frac{V^2}{2}$ which falls onto the conditions of the proposed theorem. ■

A. Horizontal alignment

Although the proposed controlled only guarantees that the error is ultimately bounded, it is possible to prove that the error in the lateral direction converges to zero exponentially. The horizontal alignment error is given by

$$\delta_2 = \pi_{q^*}\bar{\delta} = \pi_{q^*}\sum \frac{\bar{H}_i}{\|\bar{H}_i\|}. \tag{61}$$

Assuming that q^* satisfies (45), δ_2 can also be expressed as

$$\delta_2 = -u_0 u_0^T \sum \frac{\bar{H}_i}{\|\bar{H}_i\|}. \tag{62}$$

The following lemma establishes a relation between $\sum \frac{\bar{H}_i}{\|\bar{H}_i\|}$ and $\sum \bar{H}_i$ and shows that we can use a new representation for the horizontal alignment error given by

$$\phi = \frac{1}{n}u_0^T \sum \bar{H}_i. \tag{63}$$

Lemma 1: Assume that $q(t)^T q^* > 0$ for all $t > t_0$ and let

$$\begin{cases} \theta = \frac{u_0^T \sum \frac{\bar{H}_i}{\|\bar{H}_i\|}}{\phi}, & \text{for} \quad \phi \neq 0 \\ \theta = \frac{n^2}{\sum \bar{H}_i}, & \text{for} \quad \phi = 0 \end{cases} \tag{64}$$

then, $\delta_2 = -\phi\theta u_0$, $\theta > 0$ and $\phi = 0 \Leftrightarrow \delta_2 = 0$.

Proof: Consider the case where we have two parallel lines, as shown in Fig. 6 Notice that $u_0^T \bar{H}_i = u_1^T \pi_u \bar{p}_i$ and consider, from now on, the abuse of notation

$$p_i = \pi_u \bar{p}_i \tag{65}$$

Hence we want to prove that

$$\sum u_1^T \frac{p_i}{\|p_i\|} = \phi \sum u_1^T p_i,\ \phi > 0 \tag{66}$$

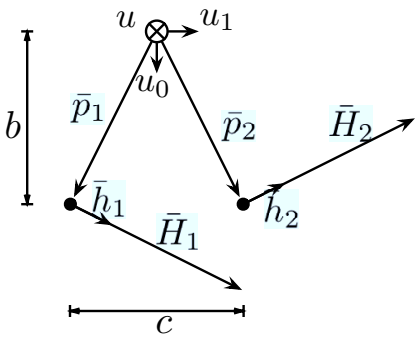

Fig. 6. Reference frames.

Firstly, consider the case where

$$\sum u_1^T p_i = 0 \Leftrightarrow \sum u_1^T \frac{p_i}{\|p_i\|} = 0 \tag{67}$$

this is the case in Fig. 6, where the camera is in the center of the lines. It is simple to verify that

$$\begin{cases} p_1 = bu_0 - \frac{c}{2}u_1 \\ p_2 = bu_0 + \frac{c}{2}u_1 \end{cases} \tag{68}$$

and $\|p_1\| = \|p_2\|$, and consequently

$$\frac{1}{\|p_1\|}\sum u_1^T p_i = \theta \sum u_1^T p_1 \Rightarrow \theta = \frac{1}{\|p_1\|} = \frac{1}{\|p_2\|} > 0. \tag{69}$$

Now, consider the case where $\sum u_1^T p_i \neq 0$. For this case it is possible to write

$$\theta = \frac{\sum u_1^T \frac{p_i}{\|p_i\|}}{\sum u_1^T p_i} \tag{70}$$

and it remains to be proven that $\theta > 0$. Consider the case where $\sum u_1^T p_i > 0$, then necessarily we have

$$u_1^T p_1 > -u_1^T p_2 \quad \Leftrightarrow \quad u_1^T p_1 = -\frac{c}{2} + \varepsilon, \varepsilon > 0 \tag{71}$$

$$u_1^T p_2 = \frac{c}{2} + \varepsilon \tag{72}$$

From the image it is easy to verify that $c = -2u_1^T p_1$ when the camera is in the middle of the two lines, hence

$$\frac{u_1^T p_1}{\|p_1\|} = \frac{-\frac{c}{2} + \varepsilon}{b^2 + \left(-\frac{c}{2} + \varepsilon\right)^2} \tag{73}$$

$$\frac{u_1^T p_2}{\|p_2\|} = \frac{\frac{c}{2} + \varepsilon}{b^2 + \left(\frac{c}{2} + \varepsilon\right)^2} \tag{74}$$

The necessary condition can be written as

$$\left(\frac{u_1^T p_1}{\|p_1\|}\right)^2 < \left(\frac{u_1^T p_2}{\|p_2\|}\right)^2 \Leftrightarrow \tag{75}$$

$$\Leftrightarrow \frac{\left(-\frac{c}{2} + \varepsilon\right)^2}{b^2 + \left(\frac{c}{2} - \varepsilon\right)^2} < \frac{\left(\frac{c}{2} + \varepsilon\right)^2}{b^2 + \left(\frac{c}{2} + \varepsilon\right)^2} \Rightarrow \tag{76}$$

$$\Rightarrow \varepsilon > 0 \wedge b \neq 0 \tag{77}$$

The resulting condition $b = 0$ is not an issue, since the restrictions defined on matrix Q to avoid ill-conditioning of the control synthesis, require the camera to be above the lines by some distance greater than zero. Analogously, for the case $\sum u_1^T p_i < 0$, we can follow the same line-of-thought, and the resulting condition is the same.

This result can be easily extended for the generic case where n lines are considered, but the notation is much heavier. ■

To show that ϕ converges to zero we can apply the backstepping technique to obtain

$$\dot{\phi} = -k_4\phi + \phi_v \tag{78}$$

where $\phi_v = u_0^T \mathrm{s_k}(u)\, v + k_4\phi$. The derivative of ϕ_v is given by

$$\dot{\phi}_v = u_0^T \mathrm{s_k}(u)\, \mathrm{s_k}(v)\, u_a - k_4^2\phi + k_4\phi_v. \tag{79}$$

Using the control law for u_a defined in Theorem 1, and noting that

$$u_0^T \mathrm{s_k}(u)\, \mathrm{s_k}(v)\, u_a = -k_3\left(u_0^T \mathrm{s_k}(u)\, v - \theta k_1\phi\right) \tag{80}$$

we can write

$$\dot{\phi}_v = -(k_3(k_1\theta - k_4) + k_4^2)\phi - (k_3 - k_4)\phi_v. \tag{81}$$

Proposition 1: Consider the dynamics given by (78) and (81). Then, there exist gains k_3 and k_4 such that origin of the system is exponentially stable.

The proof of this proposition is based on the following Lyapunov function

$$V_y = \frac{k_4^2}{2}\|\phi\|^2 + \frac{1}{2}\|\phi_v\|^2 \tag{82}$$

whose derivative is given by

$$\dot{V}_y = -k_4^4\|\phi\|^2 + -k_3\left(k_1\theta - k_4\right)\phi_v^T\phi - (k_3 - k_4)\|\phi_v\|^2. \tag{83}$$

From Theorem 1, $\bar{\delta}$ is bounded and consequently δ_2 and ϕ are also bounded, hence θ is bounded. Therefore it can be shown that there exist a set of gains that ensure that $\dot{V}_y$ is negative definite.

V. Simulation Results

The IBVS control scheme described is simulated using the UAV model described in Section II. The aircraft model incorporates the nonlinear flight dynamics including aerodynamic effects and saturation on control surfaces deflection and thrust. Simulations have been undertaken resorting to Simulink®. The control scheme used is represented in Figure 7. The camera simulator (see Figure 7) generates the

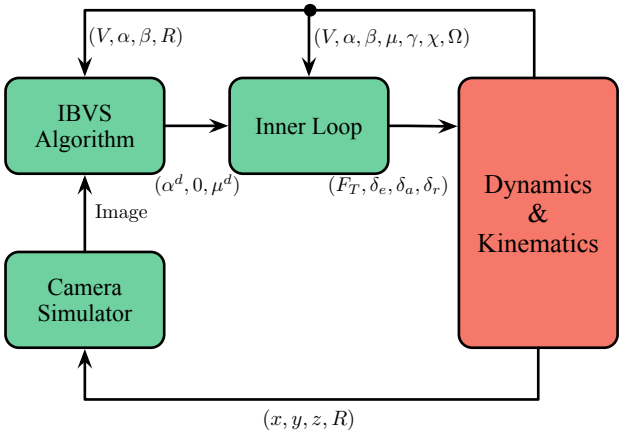

Fig. 7. Simulation scheme.

image seen by the airplane's camera at a fixed frequency of 20 frames per second. Every time that each new frame is generated, the IBVS controller is triggered and the algorithm is applied.

In the simulations presented, the airplane is set to follow a pair of catenary lines in the presence of a constant wind disturbance.

The lines are aligned with the x-axis of the inertial coordinate frame $\{\mathcal{I}\}$ at an average height of 10 meters above the ground. Figures 8, 9 and 10 show the results obtained with $k_1 = 1$ and $k_2 = 0.01$. The desired velocity that the inner-loop maintains is the nominal velocity for the aircraft's model presented, $9.11\ \mathrm{ms}^{-1}$. The wind intensity throughout the simulations is of $1\ \mathrm{ms}^{-1}$ which is more than $10\ \%$ of the relative airspeed velocity.

Figure 11 shows the 3-D path described by the aircraft with the representation of the curves that are being followed. The results show that the algorithm presented suits the application proposed. After an initial transient, the position error converges to zero in the horizontal direction and is bounded in the vertical direction. As discussed in Section IV, the trajectory described by the vehicle reflects the averaging effect of the IBVS guidance controller, which is acting as a first order filter on the curvature of the lines given by $|\frac{\partial\sigma(\tau_\xi)}{\partial\tau}|$. As illustrated in Figure 12, reducing the curvature's variation allows for considerable a improvement in position tracking.

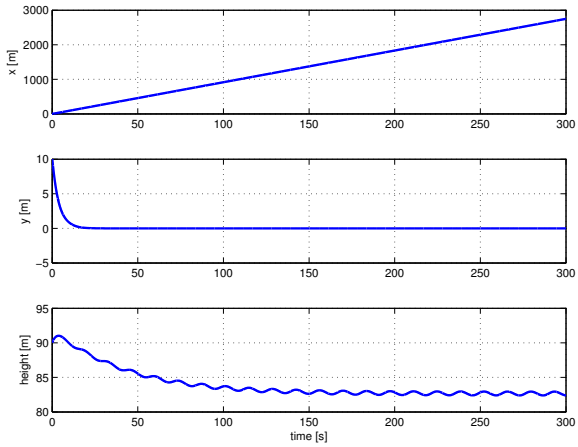

Fig. 8. Aircraft's position $(x, y, |z|)$.

VI. Concluding Remarks

This paper proposed a nonlinear IBVS controller scheme for fixed-wing aircraft, without direct measurement of the aircraft position. The proposed controller allows the UAV to follow a set of parallel non-straight lines in 3-D space. The algorithm presented has been theoretically proved and tested in simulation with a nonlinear model of an UAV. Results show that the control approach is suitable for the task and is robust to wind gust.

Future work includes image treatment in the simulation architecture, using images from a flight simulator such as FlightGear®. Also simulations with other types of wind gust models, such as Dryden spectrum are planed. The inclusion of a pan & tilt camera to ensure that the target surface is always visible is also one of the goals for future work.

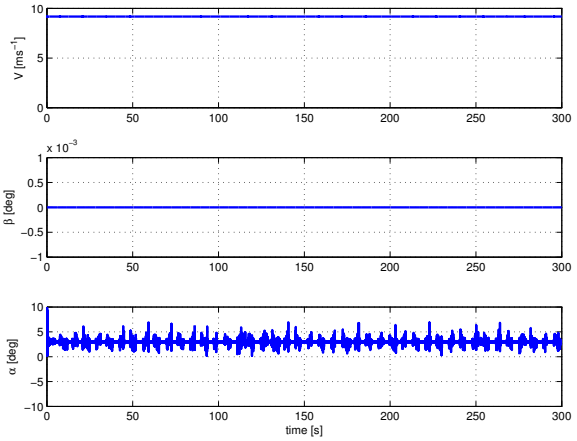

Fig. 9. Relative airspeed magnitude and direction (V, β, α).

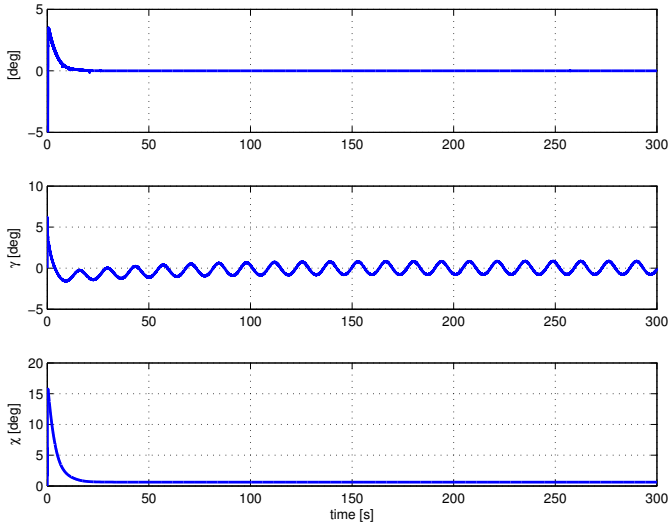

Fig. 10. Aircraft's attitude (μ, γ, χ).

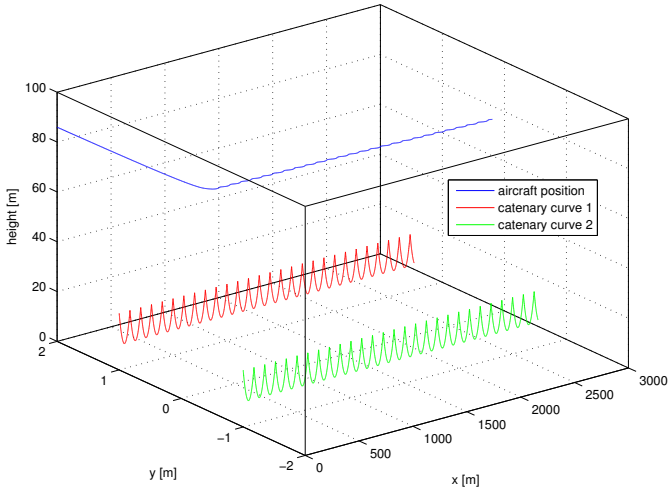

Fig. 11. 3-D path described by the aircraft.

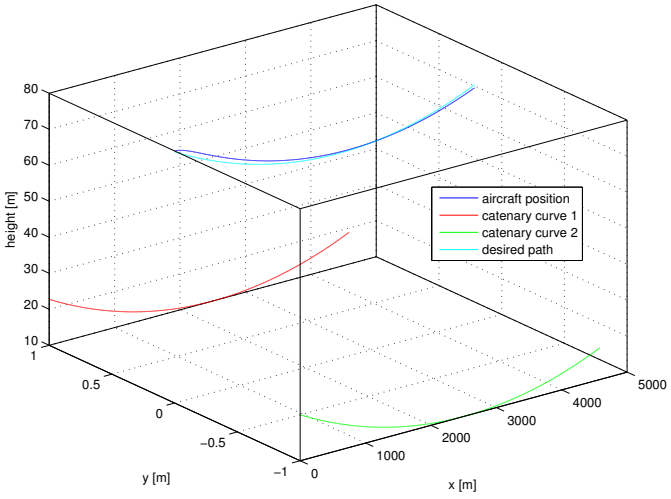

Fig. 12. 3-D path described by the aircraft following slowly varying catenaries.

REFERENCES

[1] N. Metni, T. Hamel, and F. Derkx, "Visual tracking control of aerial robotic systems with adaptive depth estimation," in *Decision and Control, 2005 and 2005 European Control Conference. CDC-ECC '05. 44th IEEE Conference on*, 2005, pp. 6078 – 6084.

[2] B. Guerreiro, C. Silvestre, R. Cunha, and D. Antunes, "Trajectory tracking H2 controller for autonomous helicopters: an application to industrial chimney inspection," in *17th IFAC Symposium on Automatic Control in Aerospace*. ONERA, IFAC, June 2007.

[3] F. Chaumette and S. Hutchinson, "Visual servo control, part i: Basic approaches," *IEEE Robotics and Automation Magazine*, vol. 13, no. 4, pp. 82–90, December 2006.

[4] ——, "Visual servo control, part ii: Advanced approaches," *IEEE Robotics and Automation Magazine*, vol. 14, no. 1, pp. 109–118, March 2007.

[5] N. Guenard, T. Hamel, and R. Mahony, "A practical visual servo control for an unmanned aerial vehicle," *Robotics, IEEE Transactions on*, vol. 24, no. 2, pp. 331 –340, April 2008.

[6] R. Mahony and T. Hamel, "Image-based visual servo control of aerial robotic systems using linear image features," *Robotics, IEEE Transactions on*, vol. 21, no. 2, pp. 227–239, April 2005.

[7] F. Le Bras, T. Hamel, C. Barat, and R. Mahony, "Nonlinear image-based visual servo controller for automatic landing guidance of a fixed-wing aircraft," in *European Control Conference*, Aug. 2009, pp. 1836–1841.

[8] P. Serra, F. Le Bras, T. Hamel, C. Silvestre, and R. Cunha, "Nonlinear ibvs controller for the flare maneuver of fixed-wing aircraft using optical flow," in *Decision and Control (CDC), 2010 49th IEEE Conference on*, Dec. 2010, pp. 1656 – 1661.

[9] A. Isidori, L. Marconi, and A. Serrani, *Robust Autonomous Guidance*. Secaucus, NJ, USA: Springer-Verlag New York, Inc., 2003.

[10] S. Bertrand, T. Hamel, and H. Piet-Lahanier, "Trajectory tracking of an unmanned aerial vehicle model using partial state feedback," in *European Control Conference*, 2007.

[11] B. L. Stevens and F. L. Lewis, *Aircraft Control and Simulation*. John Wiley & Sons, Inc., 2003.

[12] J. Farrell, M. Sharma, and M. Polycarpou, "Backstepping-based flight control with adaptive function approximation," *JOURNAL OF GUIDANCE, CONTROL, AND DYNAMICS*, 2005.

[13] S. Snell, D. Enns, and W. Garrard, "Nonlinear inversion flight control for a supermaneuverable aircraft," *Journal of Guidance Control and Dynamics*, vol. 15, no. 4, pp. 976–984, 1992.

[14] Z. F. Yang and W. H. Tsai, "Using parallel line information for vision-based landmark location estimation and an application to automatic helicopter landing," in *Robotics and Computer-Integrated Manufacturing*, 1998, pp. 297–306.